Available online at www.sciencedirect.com

ScienceDirect

MATTER AND RADIATION AT EXTREMES

Matter and Radiation at Extremes 1 (2016) 224–236

www.journals.elsevier.com/matter-and-radiation-at-extremes

Research article

How far away are accurate equations of state determinations? Some issues on pressure scales and non-hydrostaticity in diamond anvil cells

Lei Liu [a,b], Yan Bi [a,*]

[a] *National Key Laboratory of Shock Wave and Detonation Physics, Institute of Fluid Physics, China Academy of Engineering, Mianyang, 621900, China*
[b] *Department of Earth Science, Uppsala University, Uppsala, SE, 75236, Sweden*

Received 29 March 2016; revised 19 May 2016; accepted 27 May 2016
Available online 21 June 2016

Abstract

The equations of state (EOSs) of materials are the cornerstone of condensed matter physics, material science, and geophysics. However, acquiring an accurate EOS in diamond anvil cell (DAC) experiments continues to prove problematic because the current lack of an accurate pressure scale with clarified sources of uncertainty makes it difficult to determine a precise pressure value at high pressure, and non-hydrostaticity affects both the volume and pressure determination. This study will discuss the advantages and drawbacks of various pressure scales, and propose an absolute pressure scale and correction methods for the effects of non-hydrostaticity. At the end of this paper, we analyze the accuracy of the determined EOS in the DAC experiments we can achieve to date.

PACS codes: 62.50.-p; 64.30.-t; 07.35.+k

Keywords: Equation of state; Pressure scale; Nonhydrostaticity effect; Diamond anvil cell

1. Introduction

The equations of state (EOSs), which link the thermodynamic variables (pressure, temperature, volume, *etc*.) of materials, are of great interest to condensed matter physicists, material scientists, and geophysicists. The EOSs of materials are appropriate benchmarks for testing the validity of various theoretical models in condensed matter physics. In geophysics, the EOSs of the candidate minerals in the Earth's interior are indispensable for building its compositional model.

Benefiting from the developments of synchrotron X-ray diffraction (XRD) and double-sided laser heating techniques in the past decades, the diamond anvil cell (DAC) is routinely used to determine the EOS of materials up to 100 GPa and 3000 K [1]. The highest pressures and temperatures that can be achieved in DAC are up to ~750 GPa [2] and ~6000 K [3]. In laser heating DAC experiments, the pressure is determined from the pressure scales (*e.g*., known EOSs of materials, the ruby fluorescence pressure scale, or other secondary optical pressure scales); the temperature is determined from the thermal radiation spectrum of samples; and the volume is determined from the X-ray diffraction patterns of samples [1].

In this paper, we focus on EOS determination under ambient temperatures. Currently, the uncertainties of pressure scales and the effects of non-hydrostaticity in DAC prevent us from achieving accurate EOS. We attempt to address the uncertainties of various pressure scales, and analyze the non-hydrostaticity effects quantitatively in volume determination (and subsequently the pressure determination) of materials by XRD technique under high pressures.

* Corresponding author.
E-mail address: biyan@hpstar.ac.cn (Y. Bi).
Peer review under responsibility of Science and Technology Information Center, China Academy of Engineering Physics.

http://dx.doi.org/10.1016/j.mre.2016.06.002

This paper is organized in three parts: various pressure scales and their advantages and disadvantages are summarized and discussed in Section 2; the effects of non-hydrostaticity and methods to correct them in DAC XRD experiments are discussed in Section 3; and in Section 4, we analyze the accuracy of the determined EOSs we can achieve to date.

2. Pressure scale

There are two categories of pressure scales in DAC experiments: (1) the known EOSs of materials derived from experiments (ultrasonic [4–7], shock-wave [8–10], Brillouin scattering and X-ray diffraction [11], *etc*.) or theoretical calculations (thermodynamic calculations [12,13] and density function theory (DFT) calculations [14,15]); and (2) the pressure scales calibrated against the known EOSs of materials, especially the optical pressure scales (fluorescence of ruby [16,17] and SrB_4O_7:Sm^{2+} (SBO) [18–20], Raman signal of diamond [21–24] and *c*-BN [25–27], *etc*.). The first category of pressure scales is impractical in bench-top experiments, where high intensity X-ray is often unavailable, whereas the calibrated optical pressure scales are widely used. Generally, pressure standard candidates have simple and stable crystal structures in a wide pressure and temperature range, and are chemically inert to the samples and pressure transmitting media (PTM). This section introduces how various pressure scales were established, and discusses the advantages and disadvantages of each pressure scale. At the end of this section, we propose an absolute pressure scale with refined sources of uncertainty.

2.1. Known EOS of candidate materials

2.1.1. Analytical EOS and ultrasonic determination

The elastic constants and subsequently the bulk moduli of materials can be derived by determining their acoustic wave propagation velocities in single crystals along different directions, with ultrasonic techniques. Fitting the obtained pressure-bulk modulus data provides constrains on the pressure derivative of the bulk modulus. Basically, this is the normal approach to obtain materials' accurate bulk moduli and its pressure derivatives. Unfortunately, traditional ultrasonic techniques are limited in low pressure ranges, usually below 20 GPa [28]. However, recent advances in gigahertz ultrasonic techniques [29], laser ultrasonic techniques [30], and inelastic X-ray scattering techniques [31] in DAC experiments have extended the pressure limit to mega-bar range.

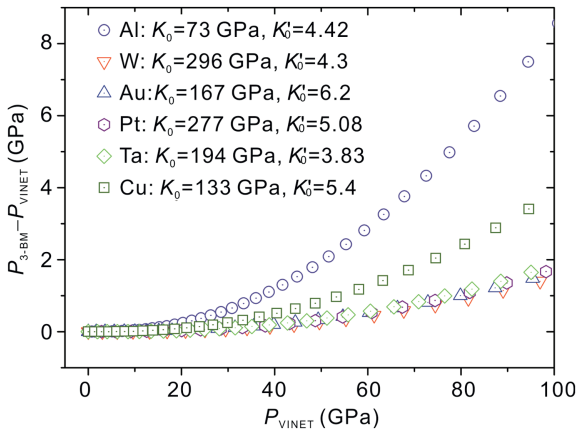

Fig. 1. The pressure difference of Al, W, Au, Pt, Ta, and Cu, when using the same K_0 and K_0' values but different EOS formulas. The K_0 and K_0' values determined by ultrasonic techniques are from Ref. [4] for Al, Ref. [7] for W, Ref. [5] for Au, Ref. [37] for Pt, Ref. [6] for Ta and Ref. [5,38] for Cu respectively.

The obtained bulk modulus and its pressure derivatives are plugged into EOS formulas to describe the compressive behavior of materials under higher pressures. The most widely used EOS formulas are the third-order Birch–Murnaghan EOS (3-BM) [32,33]:

$$P=\frac{3K_0}{2}\left[\left(\frac{V}{V_0}\right)^{-7/3}-\left(\frac{V}{V_0}\right)^{-5/3}\right]\times\left\{1+\frac{3}{4}\left(K_0^{'}-4\right)\left[\left(\frac{V}{V_0}\right)^{-2/3}-1\right]\right\} \quad (1)$$

and the Vinet EOS [34,35].

$$P=3K_0\left(\frac{V}{V_0}\right)^{-2/3}\left[1-\left(\frac{V}{V_0}\right)^{1/3}\right]\times\exp\left\{\frac{3}{2}\left(K_0'-1\right)\left[1-\left(\frac{V}{V_0}\right)^{1/3}\right]\right\} \quad (2)$$

where V, V_0, K_0 and K_0' are the volume at pressure P, the volume at ambient pressure, the bulk modulus at atmospheric pressure, and the pressure derivative of the bulk modulus, respectively. We are now concerned with the following question: for a material with given volume V, are there any differences in pressure if we use the same K_0 and K_0' values but different EOS formulas to calculate its pressure? We calculated the isotherms of six widely-used pressure standard materials (Al, W, Au, Pt, Ta and Cu) with the 3-BM and Vinet EOS formulas respectively, using the same K_0 and K_0' values. The pressure differences for each material are illustrated in Fig. 1. The 3-BM EOS formula gives a higher pressure for all six materials. Below ~20 GPa, the two EOS formulas give consistent pressures. However, the pressure difference reaches ~8% for Al, ~4% for Cu, and less than 2% for W, Au, Pt and Ta at 100 GPa. These pressure differences cannot be ignored, especially for Al and Cu. This result demonstrates that we must carefully choose appropriate EOS formulas to describe the compressive behavior of materials. The Vinet EOS formula, derived from an empirical inter-atomic potential, is more suitable to describe compressible solids under high pressures [36].

2.1.2. Shock-wave reduced isotherms (SWRIs)

(1) Grüneisen framework

The isotherms reduced from the Hugoniot curve within the framework of the Grüneisen EOS or Grüneisen function [9,16,39] are:

$$P_{300} = P_{\mathrm{H}} - (\gamma/V)(E_{\mathrm{H}} - E_{300}) = P_{\mathrm{H}} - P_T \tag{3}$$

where γ is the Grüneisen parameter and E_{300} is the specific isothermal energy at V and 300 K. The specific Hugoniot energy is given by:

$$E_{\mathrm{H}} = \frac{1}{2}P_{\mathrm{H}}(V_0 - V) \tag{4}$$

E_{300} consists of two parts: the compressional energy along the 0 K isotherm plus the thermal energy required to raise the temperature to 300 K. For example:

$$E_{300} = -\int_{V_0}^{V} P_{0\mathrm{K}}\mathrm{d}V + \int_{0}^{300} C_V(T)\mathrm{d}V \tag{5}$$

where C_V is the specific heat at constant volume. The pressure along the 0 K isotherm $P_{0\mathrm{K}}$ can be determined again by employing the Grüneisen EOS:

$$P_{0\mathrm{K}} = P_{\mathrm{H}} - (\gamma/V)\left(E_{\mathrm{H}} - \int_{V_0}^{V} P_{0\mathrm{K}}\mathrm{d}V\right). \tag{6}$$

(2) Mean-field potential (MFP) approach [40–42]

The Helmholtz free-energy $F(V,T)$ per ion at certain volumes V and temperatures T can be written as:

$$F(V,T) = E_{\mathrm{c}}(V) + F_{\mathrm{ion}}(V,T) + F_{\mathrm{el}}(V,T) \tag{7}$$

where $E_{\mathrm{c}}(V)$ is the total energy at 0 K, F_{ion} is the vibration-free energy of lattice ions, and F_{el} is the free energy arising from the thermal excitation of electrons. The $E_{\mathrm{c}}(V)$ is calculated within the framework of the full-potential linearized augmented plane-wave (LAPW) method. The F_{ion} is estimated using the mean-field potential:

$$g(r,V) = \frac{1}{2}[E_{\mathrm{c}}(R+r) + E_{\mathrm{c}}(R-r) - 2E_{\mathrm{c}}(R)] \tag{8}$$

where R is equilibrium position of lattice ion and r is the deviate distance from R. The Hugoniot curves *viz.* $P(X)$, where X is the volume compression ratio, describes the relationship of pressure and volume under shock compression. The experimental shock-wave data $X_{\mathrm{sw}}^{\mathrm{ex}}(P)$ can be expressed as:

$$X_{\mathrm{sw}}^{\mathrm{ex}}(P) = X_{300}^{\mathrm{ex}}(P) + X_{\mathrm{th}}^{\mathrm{ex}}(P) \tag{9}$$

where X_{300}^{ex} is the experimental 300 K isotherm and $X_{\mathrm{th}}^{\mathrm{ex}}$ is the volume expansion of the principal Hugoniot curve, relative to 300 K isotherm. Accordingly, the calculated results of the MFP approach can also be written in the equivalent form:

$$X_{\mathrm{sw}}^{\mathrm{MFP}}(P) = X_{300}^{\mathrm{MFP}}(P) + X_{\mathrm{th}}^{\mathrm{MFP}}(P). \tag{10}$$

Following the MFP approach, the $X_{\mathrm{sw}}^{\mathrm{MFP}}$ and X_{300}^{MFP} can be easily calculated. The reduced 300 K EOS from Hugoniot data can be obtained using the following form:

$$X_{300}^{\mathrm{rd}}(P) \approx X_{300}^{\mathrm{ex}}(P) = X_{\mathrm{sw}}^{\mathrm{ex}}(P) - \left[X_{\mathrm{sw}}^{\mathrm{MFP}}(P) - X_{300}^{\mathrm{MFP}}(P)\right] \tag{11}$$

Hozapfel [13] pointed out that the theoretical models used to derive SWRIs from Hugoniot data did not usually take into account the following effects: anharmonicity, dispersion in the Grüneisen parameters, and the creation of defects, *etc*. Hozapfel also considered that different models were required for materials in different states (solid states, fluid states, and their mixed states) [13]. The temperature and thermal pressure introduced in the isentropic compression are significantly lower than Hugoniot, thus Chijioke et al. recommended that the isentropes were better reference curves than Hugoniot for deriving more accurate 300 K isotherms [43]. The Hugoniot, isentrope and isotherm are compared schematically in Fig. 2.

2.1.3. Thermodynamic deduced isotherms (TDDIs)

(1) Dorogokupets and Oganov's work [12]

Dorogokupets and Oganov tried to construct a semi-empirical EOS to describe the compressive behaviors of materials in wide pressure and temperature ranges, based on shock-wave, ultrasonic, X-ray diffraction, and thermochemical data. They wrote the Helmholtz free energy as the sum of six parts:

$$F = U_0 + E(V) + F_{\mathrm{qh}}(V,T) + F_{\mathrm{anh}}(V,T) + F_{\mathrm{el}}(V,T) + F_{\mathrm{def}}(V,T) \tag{12}$$

where U_0 is the reference energy, $E(V)$ is the cold part of the free energy at reference conditions (ambient condition, for example), and $F_{\mathrm{qh}}(V,T)$, $F_{\mathrm{anh}}(V,T)$, $F_{\mathrm{el}}(V,T)$ and $F_{\mathrm{def}}(V,T)$ are the quasi-harmonic part, intrinsic anharmonic part, electronic contribution, and thermal defect contribution to the Helmholtz free energy, respectively. The latter five parts of Eq. (12) are analytic. Eq. (12) is universal and 22 parameters are needed to define the Helmholtz free energy of a specific material. By fitting it to the accurate experiment data, unbiased by pressure calibration (heat capacity, relative enthalpy, volume, thermal expansion, adiabatic bulk modulus at zero pressure and various temperatures, Hugoniot pressure at specific

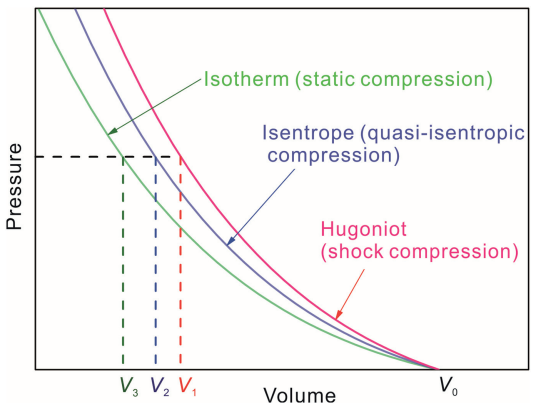

Fig. 2. A schematic comparison of Hugoniot, isentrope, and isotherm.

compression, *etc*.), the 22 parameters are acquired, and the EOS of a specific material can be calculated.

(2) Holzapfel's work [13]

By further considering the dispersion in mode-Grüneisen parameters and anharmonic phonon contributions to free energy, thermophysical data at low pressure and especially temperature dependence on bulk moduli at ambient pressure $K_0'(T)$, is used to constrain a thermodynamic model for EOSs in wide ranges of pressure and temperature. Using the constrained model, the EOSs of Cu, Ag, and Au were obtained.

(3) Jin's work [44,45]

Jin et al. calculated the thermal EOSs of MgO, Au and Pt using the Hugoniot data within the Mie–Grüneisen framework. The bulk moduli and their pressure derivatives of the materials at 0 K are derived from the 300 K Hugoniot parameters, and then plugged into a special EOS formula to obtain their 0 K isotherms. By adding the thermal pressure relative to the 0 K isotherm at given temperature, the thermal EOSs of materials are acquired. This procedure has an advantage of calculating the 0 K isotherm, following Wu's approach [46], which is an analytic and convenient method to calculate the 0 K isotherm.

Dorogokupets [12] and Holzapfel [13] both present appropriate constrained thermodynamic models for the EOSs of materials, especially for metals. Generally, the EOSs derived from the constrained thermodynamic model are reliable and have less uncertainties. However, the thermophysical and/or the thermochemical data, which is used to constrain the thermodynamic model, needs to be carefully selected in order to constrain all the effects that contribute to the free energy.

2.1.4. Absolute pressure scale (APS)

In 1973, by simultaneously determining the length and transit time of a material under isotropic compression, Ruoff et al. developed a method to obtain the absolute pressure [47]:

$$P = P_0 - 3\rho_0 l_0^3 \int_{l_0}^{l} \left(\frac{1}{\tau_l^2} - \frac{4}{3\tau_s^2}\right)\left[\frac{1}{1+\Delta(P)}\right]\frac{\mathrm{d}l}{l^2} \tag{13}$$

where

$$\Delta(P) = \frac{\beta^2 B_S T}{\rho C_P}, \tag{14}$$

ρ_0, l_0 are the density and length of material at ambient pressure; τ_l and τ_s are the travel time of the longitudinal wave and shear wave, respectively. β, B_S, T, C_P are the volume thermal expansion coefficient, adiabatic bulk modulus, absolute temperature, and specific heat, respectively. Eq. (13) denotes that if l, τ_l, and τ_s are measured simultaneously, the absolute pressure can be determined. Obviously, there were two drawbacks of this method in the 1970s: (1) there was no method to measure the length of materials under compression directly; and (2) the pressure range that the ultrasonic technique could achieve was too low. These two disadvantages were overcome by Li et al. in 2005 [48]. By simultaneously measuring the travel time with an ultrasonic technique, the density by X-ray diffraction (XRD), and the length by X-ray radiography, Li et al. developed an absolute pressure scale of NaCl EOS up to 20 GPa.

Later, Xu et al. [49] proposed an approach to achieve an accurate EOS of materials by combining the Brillouin scattering and single crystal X-ray diffraction techniques, without any theoretical assumptions:

$$P = -\int_{V_0}^{V} \frac{K_T(V')}{V'}\mathrm{d}V' \tag{15}$$

The $K_T(V')$ relationship is acquired by performing the XRD and Brillouin scattering determinations on the sample under the same loading environment. The volume of the sample is determined by the XRD technique. For Brillouin scattering experiments, the elastic wave velocities along different specific crystal directions of transparent single crystals are determined. Then the elastic constants and subsequently the adiabatic bulk modulus K_S is derived from the velocities. The isothermal bulk modulus K_T is calculated from K_S using the following relationship:

$$K_T = K_S/(1+\alpha\gamma T) \tag{16}$$

where α and γ are the thermal expansivity, and Mie–Grüneisen parameter, respectively. It is a challenge to determine accurate γ under high pressure. Consequently, the uncertainty is introduced during the transformation from K_S to K_T. This uncertainty is amplified by integration [50]. This is one of the inherent drawbacks of this approach, and another one is that the Brillouin scattering determination is only feasible for an optically transparent sample.

The EOS established after this proposal was regarded as an absolute pressure scale (APS) because no theoretical assumptions were involved. Zha et al. [11] established an EOS of MgO following Xu's proposal [49]. However, Zha et al. used single crystal samples for Brillouin scattering determination, but powder samples for XRD experiments [11]. The ruby fluorescence shift was used to bridge the adiabatic bulk modulus and the volume of MgO. This experimental procedure introduced two problems: (1) the samples were in two different sample chambers and stress environment difference must be carefully analyzed; and (2) the responses of polycrystalline versus single crystals to uniaxial loading in a DAC may be different.

The EOS of cubic SiC was established by simultaneously determining its acoustic velocities and density on single crystal samples, without referring to any prior pressure scale, up to 65 GPa with a precision of 2%–4% [51]. They believed the main source of uncertainty came from the Brillouin spectroscopy, the accuracy of which is ±200 m/s, corresponding to the 2%–4% uncertainty of the elastic moduli of

cubic SiC. Meanwhile, the conversion from K_S to K_T introduced a negligible uncertainty of ~0.05% at room temperature. Goncharov et al. extended this route to high temperature and established the *c*-BN pressure scale up to 723 K [27].

2.1.5. DFT calculated EOS

The DFT calculation results are "exact" if the exchange-correlation energy of a material is known exactly. However, in general, the local-density approximations (LDAs) give smaller volumes, while the generalized gradient approximations (GGAs) give larger volumes compared to the experimental values. Kunc and Syassen discovered that the derivative bulk modulus $K'(V)$ of materials was independent of the approximations used for the electronic exchange correlation, by using a simple scaling of P and V, where both LDA and GGA calculations gave consistent $K'(V)$ [14]. The calculated $K'(V)$ with experimental data of V_0 and K_0 describes the EOS of materials completely.

2.2. Ruby pressure scale

2.2.1. Ruby pressure scale based on SWRIs

Since Forman et al. [52] proposed that the red-shift effect of ruby R-line fluorescence could be used as a pressure gauge in DAC experiments, the ruby pressure scale has been widely calibrated and applied [16,17]. This rapid, convenient, and precise pressure measurement technique is the dominant reason why the DAC was widely accepted and deeply impacted on high pressure research.

The most important and widely accepted ruby pressure scales (RPSs) were calibrated by Mao et al. based on the SWRIs of metals, in 1978 and 1986 respectively [16,17]. The calibration route is illustrated in Fig. 3. In 1978, the RPS was calibrated based on the SWRIs of Cu, Ag, Mo and Pd, using the methanol-ethanol mixture as pressure transmitting media (PTM), and was subsequently acknowledged as a non-hydrostatic ruby pressure scale:

$$P=\frac{A}{B}\left[\left(\frac{\lambda}{\lambda_0}\right)^B-1\right],\ A=1904\ \text{GPa},\ B=5 \tag{17}$$

where λ_0 and λ are the center wavelengths of the R1 peak of ruby fluorescence at ambient pressure and high pressure, respectively. This calibration was referred to as MBSS78 thereafter, and was named after the initials of the family names of the authors and the year the paper was published. This $P(\lambda)$ relationship was later recalibrated based on the SWRIs of Cu and Ag, using argon as a pressure transmitting medium, and obtained $A = 1904$ GPa, and $B = 7.665$. This recalibrated quasi-hydrostatic RPS (MXB86) gives higher pressures than the non-hydrostatic RPS (MBSS78) does at a given wavelength.

Mao et al. [16] pointed out that the accuracy of the Hugoniot data itself, the yield strength of the materials and validity of the theory model used to convert the Hugoniot curve to isotherm, were the dominating sources of uncertainty in the SWRIs. These uncertainties transferred to the RPS and

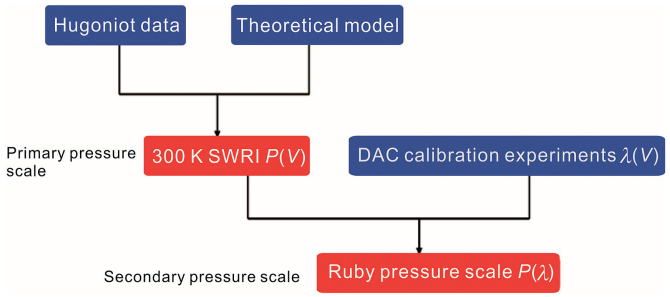

Fig. 3. The logical flow of calibrating a ruby pressure scale.

were also the focus of the consequent correction to MXB86 pressure scale [17]. In addition, logically the uncertainty of the $\lambda(V)$ relationship determined from DAC experiments and the difference between shock wave and DAC experiments are two further sources of uncertainty.

In 1987, based on the EOS of diamond, Aleksandrov et al. calibrated a new RPS (AGZS87) and pointed out that the MXB86 pressure scale underestimated pressure [53]. They also gave a new formula to describe the P-λ relationship:

$$P=A\frac{\lambda-\lambda_0}{\lambda_0}\left(1+m\frac{\lambda-\lambda_0}{\lambda_0}\right) \tag{18}$$

where $A = 1892$ GPa and $m = 6.4$. The AGZS87 pressure scale is ~16 GPa (~12%) higher than the MXB86 scale when the red shift is 40 nm. This large discrepancy was catastrophic for high pressure researchers. Since then, several investigations have focused on revealing the physical problems beneath this unacceptable discrepancy, and calibrating more accurate RPS. Some of the most important work is reviewed below:

(1) H03

In order to reconcile the discrepancy between the X-ray diffraction results based on MXB86 and the ultrasonic results at low pressure of diamond and Ta, Holzapfel considered that the MXB86 underestimated pressure and proposed a new RPS (H03, $A = 1904$ GPa, and $B = 10.4$) [54]. H03 falls between the MXB86 and AGZS87 pressure scales. Holzapfel also proposed a new form for the ruby line shift under pressure, especially at very high pressures:

$$P=\frac{A}{B+C}\left(\exp\left\{\frac{B+C}{C}\left[1-\left(\frac{\lambda-\lambda_0}{\lambda_0}\right)^{-C}\right]\right\}-1\right) \tag{19}$$

with $A = 1820$ GPa, $B = 14$ and $C = 7.3$. This form converts to Eq. (17) when C drives to zero. However, Eq. (17) is considered to be adequate for pressures below 200 GPa [15,43,55].

(2) DLM04

Dewaele et al. compared the SWRIs and the determined EOSs of six metals (Al, Cu, Ta, W, Pt, and Au) based on the MXB86 pressure scale, and revealed a systemic error [56]

which they considered arising from the underestimation of pressure by MXB86. They proposed a new pressure scale to avoid this systemic error (DLM04, $A = 1904$ GPa, and $B = 9.5$). Dorogokupets et al. regarded this correction as "revolutionary" work [12]. Actually, this work revealed the physical problems in the pressure scale calibration procedure based on SWRIs. Unfortunately, they used a mathematical approach to resolve the physical problem without enough physical constrains. The "fan" curves in Fig. 3(b) of Ref. [56] indicate intrinsic property-dependent errors from the shockwave data reduction procedure, which are not included in this systemic error. Furthermore, the SWRIs they used were reduced with different thermodynamic models and the discrepancies amongst different models are also involved in the "fan" curves. This material-dependent error needs further study. In addition, this correction result is dependent on the materials selected. In 2008, the same group recalibrated the RPS following the same procedure applied to their 2004 work (DTLM08) [57], but used SWRIs of different metals. The discrepancy reaches 1.3 GPa at the pressure of 120 GPa, just because different metals were selected in these two pressure scale calibrations.

(3) CNSS05

As highlighted by Mao et al., the strength of materials was a main source of uncertainty in SWRIs [16]. However, because of the lack of experimental strength data, the strength correction was not performed in their calibrations. Chijioke et al. calibrated a new RPS based on the SWRIs of Cu, W, Al, Au, Pt, and Ta with careful thermal pressure and strength corrections (CNSS05, $A = 1876$ GPa, $B = 10.7$) [43,58]. They also proposed new formula for RPS:

$$P = A\left[\frac{\lambda-\lambda_0}{\lambda_0} + B\left(\frac{\lambda-\lambda_0}{\lambda_0}\right)^2\right] \tag{20}$$

with $A = 1798$ GPa and $B = 8.57$.

(4) LBX13

In addition to the uncertainty of SWRIs, the non-hydrostaticity in DAC experiments, which affects the $\lambda(V)$ and consequently the $P(\lambda)$ relationship, is also an inevitable source of uncertainty in the RPS. The non-hydrostaticity effect on volume determination by the conventional X-ray diffraction method is discussed in detail in Section 3. Liu et al. revised the X-ray diffraction data which was used to calibrate the MXB86 pressure scale, and corrected the non-hydrostaticity effect on volume determination [59]. They recalibrated a new RPS based on the corrected diffraction data of Cu and Ag (LBX13, $A = 1904$ GPa, $B = 9.827$). We believe that the non-hydrostaticity or the strength effect of the PTM needs to be carefully analyzed in the RPS calibration procedure, especially when poor PTM is used.

Obviously, each correction mentioned above just focused on only one of the sources of uncertainty in the calibration procedure, as illustrated in Fig. 3. Logically, all the effects need to be taken into account to achieve a precise RPS. However, directly summing up all the corrections above will overestimate pressure because several of the corrected RPSs involved more than one effects involuntarily. For example, in CNSS05 [43], the non-hydrostaticity effect was partly avoided because a very soft PTM was used. At any rate, it is no easy job to rule out all the sources of uncertainty mentioned above to achieve an accurate RPS, following the procedure illustrated in Fig. 3.

The various RPSs are summarized in Table 1 and their discrepancies are illustrated in Fig. 4.

2.2.2. RPS based on APS

Zha et al. [11] proposed a RPS based on the absolute pressure scale of the MgO EOS (ZMH00, $A = 1904$ GPa, $B = 7.715$). ZMH00 agrees with MXB86 up to 55 GPa within a $\pm 1\%$ accuracy. However, because of the experimental drawbacks discussed in Section 2.2, it is necessary to improve ZMH00 RPS using single crystal diffraction data. Jacobsen et al. [60] performed a single crystal diffraction experiment to determine the cell volumes of MgO in helium up to 118 GPa. Unfortunately, the single crystal data was not used to establish a more accurate MgO APS, whereas they just calibrated a new RPS (JHAF08, A = 1904 GPa, B = 10.32) against the MgO APS proposed by Zha et al. [11].

In order to overcome the drawbacks of the MgO APS proposed by Zha et al., Bi and Xu performed new single crystal X-ray diffraction experiments on MgO. Combining their single crystal diffraction (Jacobsen's data below 65 GPa was included) and the Brillouin scattering data of Zha et al., they proposed a new MgO APS up to 65 GPa (BX11, $A = 1904$ GPa, $B = 9.32$), following the procedure of Xu [49] with an uncertainty of ~1.5% [61]. Furthermore, more

Table 1
Summary of RPS. There are four functional forms to describe the ruby R1 line shift with pressure, *e.g.*, Eqs. (17)–(20).

RPS	Parameters	Pressure standards	Ref
MBSS78	Eq. (17): $A = 1904$, $B = 5$	SWRIs	[16]
MXB86	Eq. (17): $A = 1904$, $B = 7.665$	SWRIs	[17]
AGZS87	Eq. (17): $A = 1918$, $B = 11.7$ Eq. (18): $A = 1892$, $B = 6.4$	Based on ultrasonic data	[53]
ZMH00	Eq. (18): $A = 1904$, $B = 7.715$	APS of MgO	[11]
H03	Eq. (18): $A = 1904$, $B = 10.8$ Eq. (19): $A = 1820$, $B = 14$, $C = 7.3$	Based on ultrasonic data	[55]
DLM04	Eq. (17): $A = 1904$, $B = 9.5$	SWRIs, eliminate systematic error	[57]
CNSS05	Eq. (17): $A = 1876$, $B = 10.71$ Eq. (20): $A = 1798$, $B = 8.57$	SWRIs with strength corrections	[44]
DO07	Eq. (18): $A = 1884$, $B = 5.5$	Semiempirical EOS	[12]
DTLM08	Eq. (17): $A = 1920$, $B = 9.61$	Eliminate systematic error	[58]
JHAF08	Eq. (17): $A = 1904$, $B = 10.32$	APS of MgO	[61]
BX11	Eq. (17): $A = 1904$, $B = 9.32$	APS of MgO	[62]
JWGC12	Eq. (17): $A = 1923$, $B = 9.75$ Eq. (18): $A = 1889$, $B = 5.48$	Calculated EOS	[45,46]
LBX13	Eq. (17): $A = 1904$, $B = 9.827$	SWRIs	[60]
ZGTD13	Eq. (17): $A = 1761$, $B = 11.92$	APS of SiC	[52]

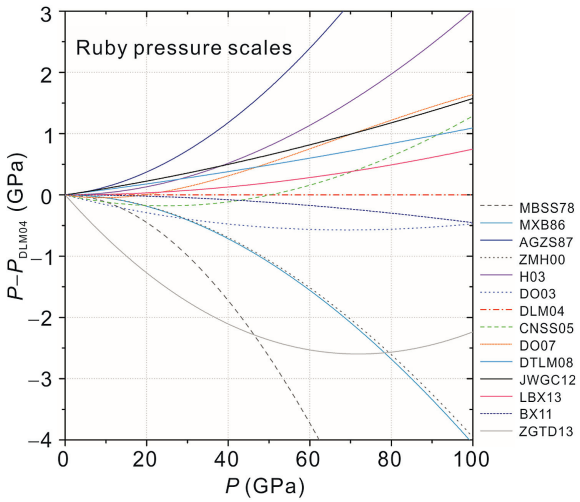

Fig. 4. Comparison of various calibrated and corrected ruby pressure scales.

accurate models were used to estimate the γ and α values at various pressures:

$$\gamma = \gamma_\infty + (\gamma_0 - \gamma_\infty)\left(\frac{V}{V_0}\right)^\beta \tag{21}$$

where $\gamma_0 = 1{,}522$, $\gamma_\infty = 1.111$ and $\beta = 4.509$ are taken from Dorogokupets and Oganov [12];

$$\alpha = \alpha_0 \exp\left[-\delta\left(1 - \frac{V}{V_0}\right)\right] \tag{22}$$

where $\alpha_0 = 3.17 \times 10^{-5}$ K^{-1} and $\delta = 4.796$. By performing the numerical integration of the $K_T(V)$ obtained from Eqs. (15), (16), (21) and (22), an absolute pressure scale can be thus established. This scale can be also expressed with a form of the Vinet equation, taking $\rho_0 = 3.586$ g/cm^3, $K_0 = 156.5$ GPa, $K_0' = 4.275$. The isothermal to adiabatic correction produces a 1.5% change at atmospheric pressure and with monotonous decreases in pressure, it becomes only 0.4% at 65 GPa.

Now we will discuss the accuracy of this APS in detail. From Eq. (15), we have:

$$\Delta P \approx -\int (\Delta K_T/K_T)(K/V)\mathrm{d}V + \int (K/V)(\Delta V/V)\mathrm{d}V \tag{23}$$

where the measuring error $\Delta K/K$ is ~0.6% in Brillouin scattering [64], and $\Delta V/V$ is ~0.3% [65], so Eq. (15) can be rewritten as:

$$\Delta P \approx 0.006\int (K_T/V)\mathrm{d}V + 0.003\int (K_T/V)\mathrm{d}V = 0.009P \tag{24}$$

Therefore, the pressure determination uncertainty $\Delta P/P$ is ~0.9%. Furthermore, the different choice of α and γ of MgO in the conversion from K_S to K_T leads to a further ~0.6% in the pressure determination. Eventually, the pressure determination uncertainty is ~1.5% for MgO APS.

Both Jacobsen and Bi used Zha's Brillouin scattering data, where the sample stress environment is complicated and additional uncertainties are consequently involved. Therefore a simultaneous X-ray diffraction and Brillouin scattering experiment performed on a specific MgO single crystal sample is still required to ensure that we acquire the bulk modulus and density of MgO under the same stress environment. A Brillouin spectrometer was installed at the 13-BM-D beamline at GSECARS of Advanced Photon Source in 2006 [62]. This unique facility is capable of establishing an absolute pressure scale, (*e.g.*, the EOS of transparent crystal) without resorting to any previous pressure scales, thus calibrating an accurate RPS.

2.2.3. Ruby pressure scale based on TDDI

Based on the EOS calculated from the thermodynamic models, Dorogokupets [12], Holzapfel [13], and Jin [44,45] calibrated the RPSs, respectively. Dorogokupets and Jin tested the validity of their materials' EOSs by showing the pressure consistency of different pressure gauges in the same run of experiments. However, it is worth mentioning that this test has an intrinsic drawback; even if the EOSs of two materials are exact and consistent with each other, the determined pressures are not consistent with each other because of the existence of non-hydrostaticity in the DAC experiments. The discrepancy between the determined pressures is determined by $(Y_{PTM}/G_{SAMPLE1} - Y_{PTM}/G_{SAMPLE2})$. The non-hydrostaticity effect in DAC experiments will be discussed in detail in Section 3.

2.2.4. Other secondary optical pressure scales

In addition to the RPS, other secondary optical pressure scales (such as the fluorescence of SrB_4O_7:Sm^{2+} (SBO), the Raman signal of *c*-BN and diamond) are alternative practical pressure scales. The SBO has four advantages over ruby to serve as a pressure standard [63]: (1) The single character of its fluorescence overcomes the R1 and R2 peak overlap problem of ruby fluorescence, which is the main determining error source of the RPS at high pressure and/or non-hydrostatic pressure; (2) It is not very sensitive to non-hydrostaticity; (3) It is softer than ruby and is more suitable for determining the pressure of soft samples because the stress concentration effect is partially avoided; (4) It is non-sensitive to temperature which is very important to determine pressure at high temperature.

Another candidate pressure scale is *c*-BN. Its intense Raman signal (which increases with increasing temperature) in addition to its stable crystal structure and chemical inertia, makes it especially suitable for high temperature studies. Temperature can be simultaneously and conveniently determined from the same Raman spectra by the intensity ratio of Stokes and anti-Stokes peaks. For example, the frequency shift of the transverse optical phonon (TO) of cubic boron nitride was calibrated to high pressures and high temperatures [25–27,64].

The Raman signal from the culet of the diamond anvil is also used as a pressure scale, especially when other pressure gauges in the sample chamber are disabled at ultrahigh pressures [21–24]. However, the $P(\nu)$ relationship of diamond is

dependent on the non-hydrostaticity, the crystallography orientation, and geometry of the anvil [24], which means that the specific $P(v)$ relationship is not universal for all determinations, and careful calibration is required before experiments.

2.3. Discussions

As Holzapfel points out, "starting from shock wave data, introduces too many uncertainties" [13]. This conclusion is easily deduced logically from Fig. 3. The TDDI EOS needs lots of experimental thermophysical and thermochemical data to constrain the thermodynamic model. The precision of the selected experimental data and what data is selected determines the validity and accuracy of the thermodynamic model, and subsequently the accuracy of the calculated EOS. Furthermore, the TDDI EOS needs to be compared with a benchmark which is independent of any prior pressure scale, before we test the validity of the theory model. Amongst the five methods to achieve the EOSs of materials discussed in Section 2.1, the APS is the most valid, accurate, and important approach, where we can recognize all the sources of uncertainty. Thus, the APS is the most appropriate benchmark to test the validity of the DFT calculation results, the thermodynamic model, and to calibrate the secondary pressure scales, like RPS for example.

To achieve a smaller uncertainty in pressure determination, we need more accurate K_T and V according to Eq. (21). For K_T, reducing the uncertainty from the Brillouin scattering experiment relies on technical development. However, we can achieve more accurate α from the thermal EOS and more accurate γ form Raman [66] and diffraction [67] experiments. More accurate α and γ will lead to a smaller level of uncertainty in the conversion from K_S to K_T. For V, the important issue of non-hydrostaticity in the DAC under high pressure needs to be carefully considered. The non-hydrodstaticity effect in DAC experiments is the topic of Section 3.

The APS is an appropriate benchmark to test the validity of other methods which are used to achieve EOSs of materials. It can also be used to calibrate other pressure gauges, EOSs of candidate materials, the ruby fluorescence pressure scale, and other secondary optical pressure scales.

3. Non-hydrostaticity and volume determination

3.1. Stress state in DAC

There are two categories of stress that the sample endures in the chamber of DAC: the microscopic stress and the macroscopic stress. The microscopic stress, *i.e.*, the deviatoric stress field throughout the sample, varies from grain to grain. The existence of microscopic deviatoric stress only broadens the X-ray diffraction peaks, but does not shift the peaks to lower or higher 2θ angles, so does not change the d-spacing values of the sample [68]. The macroscopic stress produced in the sample, which is embraced in PTM, is sketched in Fig. 5. Because of solidification of the PTM [69], the macroscopic stress is non-hydrostatic, which indicates the existence of pressure gradients (pressure varies with positions) and differential stress (pressure varies with directions). As illustrated in Fig. 5, pressure is distributed along the radial direction in the sample zone which is covered by the X-ray beam, thus the X-ray diffraction signal from this region involves the properties of the sample under different pressures. This leads to the broadening of the diffraction peaks. Differential stress means that σ_z and σ_x (or σ_y) are different throughout the sample chamber. The crystal lattice that is influenced by differential stress deforms in the following way: the lattice planes lying perpendicular to the principle stress direction σ_z are more compressed compared to those in the corresponding hydrostatic state, whereas the crystal planes lying parallel to σ_z expand due to Poisson's effect. In conventional diffraction geometry, the incident X-ray beam is nearly parallel to the stress direction σ_z. Therefore, the X-ray beam is diffracted only by the lattice planes lying nearly parallel to σ_z, and consequently, the observed d-spacing values are larger than those in corresponding hydrostatic conditions (see Fig. 6).

The broadening of the diffraction peaks arising from the pressure gradient in the sample chamber can be described as [59]:

$$\begin{aligned}\Delta\theta &= -\frac{\lambda}{6d\sqrt{1-\lambda^2/4d}}\frac{Y}{h}\frac{R}{K} \\ &= -\frac{\lambda}{6d\sqrt{1-\lambda^2/4d}}\frac{\mathrm{d}P(r)}{\mathrm{d}r}\frac{R}{K}\end{aligned} \tag{25}$$

where θ, λ, Y, h, R, K, r, and $P(r)$ are the diffraction angle, X-ray wavelength, yield strength of the sample, thickness of the sample, X-ray beam size, bulk modulus of the sample, radial distance, and pressure distribution, respectively. Eq. (25) indicates that the yield strength of the sample (or PTM, if PTM is used), the bulk modulus of the sample, the thickness of the sample, and the size of the X-ray beam all contribute to the broadening of the diffraction peaks. The maximum broadening occurs where the maximum pressure gradient appears.

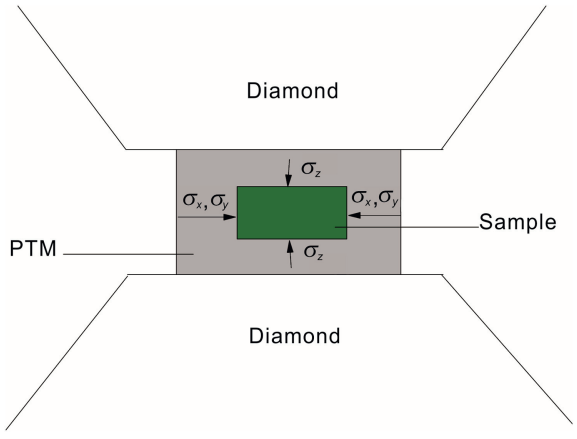

Fig. 5. Sketch map of the macroscopic stress born on the sample.

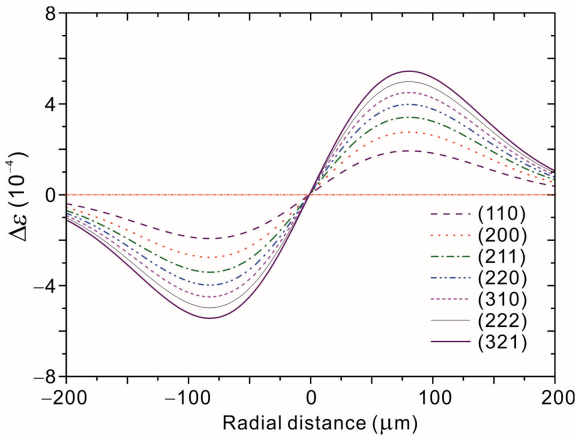

Fig. 6. Broadening widths of diffraction peaks of Mo at 21 GPa as a function of the radial distance. The pressure gradient is taken from Jin's determined results [70]. Suppose that the X-ray beam size is 10 μm and the wavelength is 0.6199 Å (the wavelength used at 4W2 High-Pressure Station of Beijing Synchrotron Facility).

Several models have been established to describe how the diffraction peaks shift quantitatively due to the differential stress in the sample chamber: the lattice strain theory and strength model will be introduced in detail in Section 3.2.

3.2. Correction of the non-hydrostaticity effect

3.2.1. Lattice strain theory [71–75]

The sophisticated lattice strain theory was established by Singh et al. to bridge the macroscopic differential stress and the microscopic lattice strain. It is based on the following three assumptions: (1) the materials are in their elastic zones; (2) the directions of the grains are randomly distributed; (3) the stress presents cylindrical symmetry, and only the diagonal terms in the stress matrix are nonzero:

$$\boldsymbol{\sigma}_{ij} = \begin{vmatrix} \sigma_1 & 0 & 0 \\ 0 & \sigma_1 & 0 \\ 0 & 0 & \sigma_3 \end{vmatrix} \tag{26}$$

Singh et al. derived the relationship between the measured d-spacing (d_{m}) and the d-spacing under corresponding hydrostatic compression (d_{p}) as the following:

$$d_{\mathrm{m}}(h,k,l) = d_{\mathrm{p}}(h,k,l)\left[1 + \left(1 - 3\cos^2\Psi\right)Q(h,k,l)\right] \tag{27}$$

$$Q(h,k,l) = (t/3)\left\{\alpha\left[2G_{\mathrm{R}}^{\mathrm{X}}(h,k,l)^{-1}\right] + (1-\alpha)(2G_{\mathrm{V}})^{-1}\right\} \tag{28}$$

Where $d_{\mathrm{m}}(h,k,l)$ is the measured d-spacing; $d_{\mathrm{p}}(h,k,l)$ is the d-spacing under corresponding hydrostatic compression; Ψ is the angle between the loading axis and the diffraction vector; $G_{\mathrm{R}}^{\mathrm{X}}$ and G_{V} are the Reuss (isostress) shear modulus and Voigt (isostrain) shear modulus, respectively; $t = \sigma_3 - \sigma_1$ is the differential stress, which is equal to the yield strength of the material in value when it yields; and α determines the relative weights of the isostress and the isostrain condition across the grain boundary.

Eq. (27) indicates that the measured lattice constants equal the lattice constants under corresponding hydrostatic compression when $1 - 3\cos^2\Psi = 0$, for example, $\Psi = 54.7°$. The radial diffraction technique was developed based on this theory to determine the hydrostatic d-spacing of materials under non-hydrostatic compression. This theory is also used to estimate the yield strength [76–78] and the elastic constants [79,80] of materials.

Recently, the value of α in specific materials was found to be larger than 1 [81], which is quite intricate for researchers. Singh considered that this was because the material underwent plastic deformation, which was not included in the framework of the lattice strain theory. Karato extended the lattice strain theory in polycrystalline sample to include the effect of plastic deformation [82]. However, Singh considered it was useless to interpret the high pressure diffraction patterns. The elastic to plastic self-consistent (EPSC) model was established by Turner and Tomé [83]. This model has been used successfully to interpret diffraction experiments, especially high pressure diffraction experiments, in which plastic deformation is undertaken [84–87].

3.2.2. Strength correction

In traditional axial diffraction geometry, the measured strain is very close to ε_x. Assuming the strains resulting from the stress are small and the materials are in their elastic region, we derived the strain difference between the true strain and the measured strain [59]:

$$\Delta\varepsilon' = \frac{\varepsilon_x + \varepsilon_y + \varepsilon_z}{3} - \varepsilon_x = \frac{Y_{\mathrm{PTM}}}{6G_{\mathrm{SAMPLE}}} \tag{29}$$

Eq. (29) indicates that $\Delta\varepsilon'$ is determined by the ratio of the yield strength of the PTM to the shear modulus of the sample: larger yield strength of the PTM and smaller shear modulus of the sample lead to a larger difference between the determined strain and the actual strain of the sample. For EOS determination, the hydrostaticity is not only determined by the yield strength of PTM, but also determined by the mechanical properties of both the PTM and the sample simultaneously. Eq. (29) can also be used as the criteria for choosing various PTMs. $\Delta\varepsilon'$ of copper, silver, platinum, molybdenum and tungsten are calculated when argon was used as the PTM, and the results are illustrated in Fig. 7.

It is worth mentioning that the yield strength value of PTM Y_{PTM} in Eq. (29) needs to be substituted by the yield strength value of the sample when no PTM is used or the sample is softer than the PTM [91].

3.2.3. Iterative correction

Radial diffraction experiments are complicated and time-consuming. By combining the line width analysis and lattice strain theory, we proposed an iterative method to avoid the non-hydrostatic effect on volume determination and obtain the

hydrostatic lattice constants accordingly [92], using the conventional diffraction technique.

(1) Line width analysis

Basing the diffraction line width on a crystalline size (with the diffraction angle as $1/\cos\theta$) and a lattice strain (with the diffraction angle as $\tan\theta$), Langford derived the following relation [93]:

$$(2\omega_{hkl}\cos\theta_{hkl})^2 = (\lambda/d)^2 + \eta_{hkl}^2\sin^2\theta_{hkl} \tag{30}$$

where $2\omega_{hkl}$, θ_{hkl}, λ, d and η_{hkl} denote the line width, the Bragg angle, X-ray wavelength, crystalline size, and microstrain, respectively. Singh et al. suggested that Eq. (30) was appropriate to analyze the high pressure diffraction pattern because the major source of the broadening is the microstrain in DAC experiments [94]. Then the microstrain η_{hkl} dependent on (h, k, l) can be obtained by the following relationship:

$$\eta_{hkl} = 4P_{\max}/E(h,k,l) \tag{31}$$

where $E(h,k,l)$ is the single crystal Young's modulus, and $P_{\max}$ is the difference between the minimum and maximum microstresses, in the microstress model proposed by Stokes and Wilson. Further studies on MgO [95], Au [96], and Fe [97] show that $2P_{\max}$ equals the differential stress t in the DAC, thus the Eq. (30) can be rewritten as:

$$(2\omega_{hkl}\cos\theta_{hkl})^2 = (\lambda/d)^2 + (2t)^2\sin^2\theta_{hkl}/E(h,k,l)^2 \tag{32}$$

The $(2\omega_{hkl}\cos\theta_{hkl})^2$ versus $\sin^2\theta_{hkl}/E(h,k,l)^2$ plots a straight line, with an intercept and slope of $(\lambda/d)^2$ and $(2t)^2$, respectively.

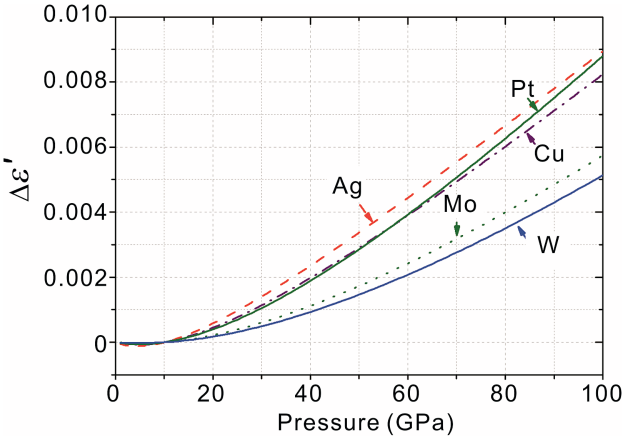

Fig. 7. Variation of $\Delta\varepsilon' = Y_{PTM}/6G_{SAMPLE}$ of copper, silver, platinum, molybdenum and tungsten versus pressure, when argon is used as the PTM. The yield strength data of argon was taken from Ref. [88]: $Y = 0.001\,P^2 - 0.01\,P$. The values of the shear moduli of Cu, Ag, Pt and W were taken from Ref. [38,89,90] and 78, respectively, and fitted with the linear function: $G_{Cu} = 47.11 + 1.35\,P$, $G_{Ag} = 29.67 + 1.38\,P$, $G_{Pt} = 62.75 + 1.077\,P$, $G_{Mo} = 123.36 + 1.38\,P$ and $G_W = 163.06 + 1.29\,P$.

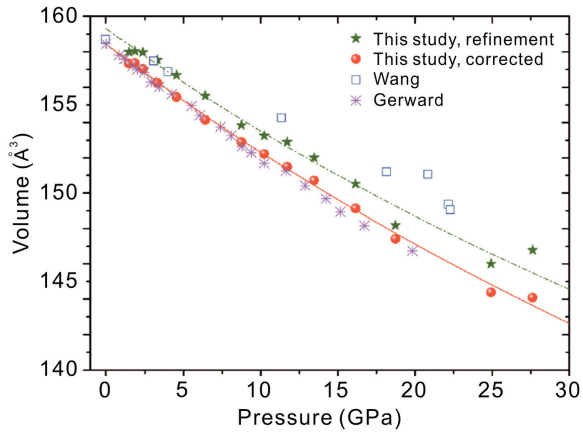

Fig. 8. The measured EOS of fluorite type CeO_2 at room temperature. Our results of bulk CeO_2 are presented by solid symbols. Green pentagrams indicate the result derived from Rietveld refinement by GSAS + EXPGUI package. Red spheres are estimated results of a_p^3 by diffraction profile widths analysis and later the iteration procedure. The open squares are the result of Wang et al. [98] of nano-CeO_2. The asterisks indicate the result of bulk CeO_2 determined by Gerward et al. [99] under quasi-hydrostatic compression. Our two sets of results are fitted with the Vinet EOS and denoted as green dash line and red solid line, respectively.

(2) Line shift analysis

In conventional diffraction geometry, the measured lattice parameter for a cubic material under a non-hydrostatic macrostress conditions satisfies the following equation:

$$a_m = M_0 + M_1\left[3\Gamma(h,k,l)\left(1 - 3\sin^2\theta_{hkl}\right)\right] \tag{33}$$

where

$$M_0 = a_p\left\{1 + (\alpha t/3)\left(1 - 3\sin^2\theta_{hkl}\right)\left[(S_{11} - S_{12}) - \left(1 - \alpha^{-1}\right)(2G_V)^{-1}\right]\right\} \tag{34}$$

$$M_1 = -a_p(\alpha S t/3) \tag{35}$$

$$\Gamma(h,k,l) = \left(h^2k^2 + k^2l^2 + l^2h^2\right)\Big/\left(h^2 + k^2 + l^2\right)^2 \tag{36}$$

$$S = S_{11} - S_{12} - S_{44}/2 \tag{37}$$

$$(2G_V)^{-1} = \frac{5(S_{11} - S_{12})S_{44}}{2[3(S_{11} - S_{12}) + S_{44}]} \tag{38}$$

a_m is the determined lattice constant, and a_p is the lattice constant under hydrostatic pressure accordingly. S_{ij} are the single crystal elastic compliances under pressure.

As discussed in Ref. [74], $M_0 \approx a_p$, and the plot of a_m versus $3\Gamma(h,k,l)(1 - 3\sin^2\theta_{hkl})$ termed as a gamma plot, is a straight line. This provides an effective method to estimate the value of αt:

$$\alpha t = -3M_1/M_0 S \tag{39}$$

(3) Estimation of a_p

In a gamma plot, the strength t can be determined from the slope of the $(2\omega_{hkl}\cos\theta_{hkl})^2$ versus $\sin^2\theta_{hkl}/E(h,k,l)^2$ plots,

and α_1 can be determined by using Eq. (39). Combining Eqs. (34) and (35), we have:

$$a_{\mathrm{p}} = M_0 + \frac{M_0}{S}\left(1 - 3\sin^2\theta_{hkl}\right)\left[(S_{11} - S_{12}) - \left(1 - \alpha^{-1}\right)(2G_{\mathrm{V}})^{-1}\right] \quad (40)$$

It is obvious that a_{p} depends on (h,k,l), which is unphysical. Considering that the θ_{hkl} ranges from ~6° to 12° in conventional experiments, and the second term varies within 3% in this θ_{hkl} range, then we replace $(1 - 3\sin^2\theta_{hkl})$ by its average $<(1 - 3\sin^2\theta_{hkl})>$ and Eq. (40) is rewritten as:

$$a_{\mathrm{p}} = M_0 + \frac{M_0}{S}<\left(1 - 3\sin^2\theta_{hkl}\right)>\left[(S_{11} - S_{12}) - \left(1 - \alpha^{-1}\right)(2G_{\mathrm{V}})^{-1}\right] \quad (41)$$

The symbol $< >$ denotes the average value derived from all the observed reflections. By putting α_1 in Eq. (31), from which a_{p1} is obtained, and substituting a_{p1} into Eq. (35), we have α_2. And then by putting α_2 in Eq. (15), we have a_{p2} and repeat this procedure until $a_{\mathrm{p}n}$ and α_n converge to a_{p0} and α_0, respectively. We then consider that a_{p0} is the lattice parameter under the according hydrostatic pressure σ_{P}.

This correction method has been applied to CeO_2 [92]. We compressed CeO_2 to about 30 GPa non-hydrostatically, and acquired the hydrostatic volume of CeO_2 by correcting the non-hydrostatic effect using this iterative method. The results are illustrated in Fig. 8. The corrected result agrees well with the hydrostatic experimental results.

4. The accuracy of determined EOSs

To achieve an accurate EOS by the diffraction technique in a DAC, we must obtain the accurate pressure and volume values of materials under pressure simultaneously. For pressure determination, we recommend the ruby pressure scale calibrated based on the MgO APS (BX11, $A = 1904$ GPa, $B = 9.32$) [61], which has an intrinsic uncertainty of ~1.5% up to 65 GPa. If a good PTM (argon, helium and so on) is used, the accuracy of the determined pressure is ~0.03 GPa [100], which accounts for a minor part in all the uncertainty of pressure under high pressure. Thus, the pressure uncertainty is ~1.5% up to 65 GPa. For volume determination, the intrinsic uncertainty of micro angular dispersive X-ray diffraction is $\Delta d/d \sim 10^{-3}$ [1], The uncertainty introduced by the non-hydrostaticity effect can be partly avoided if a good PTM (as before) is used, and determined by Eq. (27). As illustrated in Fig. 7, the non-hydrostaticity effect uncertainty achieves 9×10^{-3} if argon is used as the PTM. However, the latest results [101,102] give a much lower strength of argon, about one tenth of the value given by Mao et al. [88] at 100 GPa. Thus, the non-hydrostaticity effect introduced uncertainty is $\sim 10^{-3}$ if argon is used as the PTM. This uncertainty is even smaller if helium is used as the PTM. The volume uncertainty is not larger than $\Delta V/V \sim 10^{-2}$ if argon or helium is used as the PTM. In conclusion, we believe that, to date, we can measure an EOS of a specific material with the pressure uncertainty of 1.5%, and the volume uncertainty on the order of 10^{-3}, up to 65 GPa.

Acknowledgments

The authors thank two anonymous reviewers for their thoughtful and instructive reviews; Jian Xu for valuable discussions; Jinzhu Hu and Jinfu Shu for their experimental assistance during the MgO APS calibration. We also thank Freyja O'Toole for polishing the manuscript. This work is supported by the National Natural Science Foundation of China under Grant No. 11504354 and Research Foundation of National Key Laboratory of Shock Wave and Detonation Physics under Grants No. 9140C6703010703 and 9140C6703010803. Part of the experiments were performed at X17C in NSLS, Brookhaven National Laboratory and at the 4W2 high pressure station of BSRF (Grant Nos. KJCX2-SW-N03 and KJCX2-SW-N20).

References

[1] G. Shen, P. Chow, Y. Xiao, S. Sinogeikin, Y. Meng, et al., HPCAT: an integrated high pressure synchrotron facility at the advanced photon source, High Press. Res. 28 (2008) 145.
[2] L. Dubrovinsky, N. Dubrovinskaia, E. Bykova, V. Prakapenka, C. Prescher, et al., The most incompressible metal osmium at static pressures above 750 gigapascals, Nature 525 (2015) 226.
[3] S. Tateno, K. Hirose, Y. Ohishi, Y. Tatsumi, The structure of iron in Earth's inner core, Science 330 (2010) 359.
[4] K. Syassen, W.B. Holzapfel, Isothermal compression of Al and Ag to 120 kbar, J. Appl. Phys. 49 (1978) 4427.
[5] W.B. Holzapfel, Equations of state for Cu, Ag, and Au for wide ranges in temperature and pressure up to 500 GPa and above, J. Phys. Chem. Ref. Data 30 (2001) 515.
[6] K.W. Katahara, M.H. Manghnani, E.S. Fisher, Pressure derivatives of the elastic moduli of niobium and tantalum, J. Appl. Phys. 47 (1976) 434.
[7] D.J. Steiberg, Some observations regarding the pressure dependence of the bulk modulus, J. Phys. Chem. Solids 43 (1982) 1173.
[8] N.C. Holmes, J.A. Moriarty, G.R. Gathers, W.J. Nellis, The equation of state of platinum to 660 GPa (6.6 Mbar), J. Appl. Phys. 66 (1989) 2962.
[9] R.S. Hixson, J.N. Fritz, Sock compression of tungsten and molybdenum, J. Appl. Phys. 71 (1992) 1721.
[10] W.J. Nellis, J.A. Moriarty, A.C. Mitchell, M. Ross, R.G. Dandrea, et al., Metal physics at ultrahigh pressure: aluminum, copper, and lead as prototypes, Phys. Rev. Lett. 60 (1988) 1414.
[11] C.S. Zha, H.K. Mao, R.J. Hemley, Elasticity of MgO and a primary pressure scale to 55 GPa, PNAS 97 (2000) 13494.
[12] P.I. Dorogokupets, A.R. Oganov, Ruby, metals, and MgO as alternative pressure scales: a semiempirical description of shockwave, ultrasonic, X-ray, and thermochemical data at high temperatures and pressures, Phys. Rev. B 75 (2007) 024115.
[13] W.B. Holzapfel, Equations of state for Cu, Ag, and Au and problems with shock wave reduced isotherms, High Press. Res. 30 (2010) 372.
[14] K. Kunc, K. Syassen, $P(V)$ equations of state of solids: density functional theory calculations and LDA versus GGA scaling, Phys. Rev. B 81 (2010) 134102.
[15] K. Kunc, I. Loa, K. Syassen, Equation of state and phonon frequency calculations of diamond at high pressure, Phys. Rev. B 81 (68) (2003) 094107.
[16] H.K. Mao, P.M. Bell, Specific volume measurements of Cu, Mo, Pd, and Ag and calibration of the ruby R_1 fluorescence pressure gauge from 0.06 to 1 Mbar, J. Appl. Phys. 49 (1978) 3276.

[17] H.K. Mao, J. Xu, P.M. Bell, Calibration of the ruby pressure gauge to 800 kbar under quasihydrostatic conditions, J. Geophys. Res. 91 (1986) 4673.
[18] F. Datchi, R. LeToullec, P. Loubeyre, Improved calibration of the SrB_4O_7:Sm^{2+} optical pressure gauge: advantages at very high pressures and high temperatures, J. Appl. Phys. 81 (1997) 3333.
[19] S.V. Raju, J.M. Zaug, B. Chen, J. Yuan, J.W. Knight, et al., Determination of the variation of the fluorescence line positions of ruby, strontium tetraborate, alexandrite, and samarium-doped yttrium aluminum garnet with pressure and temperature, J. Appl. Phys. 110 (2011) 023521.
[20] Q. Jing, Q. Wu, L. Liu, J. Xu, Y. Bi, et al., An experimental study on SrB_4O_7:Sm^{2+} as a pressure sensor, J. Appl. Phys. 113 (2013) 023507.
[21] M.I. Eremets, Megabar high-pressure cells for Raman measurements, J. Raman Spectrosc. 34 (2003) 515.
[22] L. Sun, A.L. Ruoff, G. Stupian, Convenient optical pressure gauge for multipressure calibrated to 300 GPa, Appl. Phys. Lett. 86 (2005) 014103.
[23] Y. Akahama, H. Kawamura, Pressure calibration of diamond anvil Raman gauge to 310 GPa, J. Appl. Phys. 100 (2006) 043516.
[24] B.J. Baer, M.E. Chang, W.J. Evans, Raman shift of stressed diamond anvils: pressure calibration and culet geometry dependence, J. Appl. Phys. 104 (2008) 034504.
[25] T. Kawamoto, K.N. Matsukage, T. Nagai, K. Nishimura, T. Mataki, Raman spectroscopy of cubic boron nitride under high temperature and pressure conditions: a new optical pressure marker, Rev. Sci. Instrum. 75 (2004) 2451.
[26] A.F. Goncharov, J.C. Crowhurst, J.K. Dewhurst, S. Sharma, Raman spectroscopy of cubic boron nitride under extreme conditions of high pressure and temperature, Phys. Rev. B 72 (2005) 100104(R).
[27] A.F. Goncharov, S. Sinogeikin, J.C. Crowhurst, M. Ahart, D. Lakshtanov, et al., Cubic boron nitride as a primary calibrant for a high temperature pressure scale, High Press. Res. 27 (2007) 409.
[28] H. Spetzler, A. Shen, G. Shen, G. Herrmannsdoerfer, H. Schulze, et al., Ultrasonic measurements in a diamond anvil cell, Phys. Earth Planet. Inter. 98 (1996) 93.
[29] S.D. Jacobsen, H.A. Spetzler, H.P. Reichmann, J.R. Smyth, S.J. Mackwell, et al., Gigahertz ultrasonic interferometry at high P and T: new tools for obtaining a thermodynamic equation of state, J. Phys. Condens. Matter 14 (2002) 11525.
[30] N. Chigarev, P. Zinin, D. Mounier, A. Bulou, A. Zerr, et al., Laser ultrasonic measurements in a diamond anvil cell on Fe and the KBr pressure medium, J. Phys. Conf. Ser. 278 (2011) 012017.
[31] J. Lin, W. Sturhahn, J. Zhao, G. Shen, H.K. Mao, et al., Sound velocities of hot dense iron: Birch's law revisited, Science 308 (2005) 1892.
[32] F. Birch, Finite elastic strain of cubic crystal, Phys. Rev. 71 (1947) 809.
[33] F. Birch, Finite strain isotherm and velocities for single-crystal and polycrystalline NaCl at high pressure and 300 K, J. Geophys. Res. 95 (1978) 1257.
[34] P. Vinet, J. Ferrante, J.H. Rose, J.R. Smith, Compressibility of solids, J. Geophys. Res. 92 (1987) 9319.
[35] P. Vinet, J.H. Rose, J. Ferrante, J.R. Smith, Universal features of the equation of state of solids, J. Phys. Condens. Matter 1 (1989) 1941.
[36] J. Poirier, Introduction to the Physics of the Earth's Interior, Cambridge University Press, Cambridge, 2000, p. 78.
[37] G. Simmons, H. Wang, Single Crystal Elastic Constant and Calculated Aggregate Properties: A Handbook, MIT Press, Cambridge, 1971.
[38] W.B. Daniels, C.S. Smith, Pressure derivatives of the elastic constants of copper, silver and gold to 10000 Bars, Phys. Rev. 111 (1958) 713.
[39] J.C. Jamieson, J.N. Fritz, M.H. Manghnani, in: S. Akimoto, M.H. Manghnani (Eds.), High-pressure Research in Geophysics," of Advances in Earth and Planetary Sciences vol. 12, Center for Academic Publishing, Tokyo, 1982.
[40] Y. Wang, D. Chen, X. Zhang, Calculated equation of state of Al, Cu, Ta, Mo, and W to 1000 GPa, Phys. Rev. Lett. 84 (2000) 3220.
[41] Y. Wang, R. Ahuja, B. Johansson, Reduction of shock-wave data with mean-field potential approach, Phys. Rev. B 92 (2002) 6616.
[42] Y. Wang, Theoretical Studies of Thermodynamic Properties of Condensed Matter Under High Temperature and High Pressure, Ph.D thesis, Uppsala University, Uppsala, 2004.
[43] A.D. Chijioke, W.J. Nellis, A. Soldatov, I.F. Silvera, The ruby pressure standard to 150 GPa, J. Appl. Phys. 98 (2005) 114905.
[44] K. Jin, X. Li, Q. Wu, H. Geng, L. Cai, et al., The pressure-volume-temperature equation of state of MgO derived from shock Hugoniot data and its application as a pressure scale, J. Appl. Phys. 107 (2010) 113518.
[45] K. Jin, Q. Wu, H. Geng, X. Li, L. Cai, et al., Pressure-volume-temperature equation of state of Au and Pt up to 300 GPa and 3000 K: Internally consistent pressure scales, High Press. Res. 31 (2011) 560.
[46] Q. Wu, Studies on Equation of State and Grüneisen Parameter for Metals at High Pressures and Temperatures, Ph.D. thesis, China Academy of Engineering Physics, 2004.
[47] A.L. Ruoff, R.C. Lincoln, Y.C. Chen, High-pressure calibration with a new absolute-pressure gauge, J. Appl. Phys. 22 (1973) 310.
[48] B. Li, J. Kung, T. Uchida, Y. Wang, Pressure calibration to 20 GPa by simultaneous use of ultrasonic and X-ray techniques, J. Appl. Phys. 98 (2005) 013521.
[49] J. Xu, E. Huang, Primary pressure scale−A proposal, J. Geol. Soc. China 41 (1998) 199.
[50] K. Syassen, Ruby under pressure, High Press. Res. 28 (2008) 75.
[51] K.K. Zhuravlev, A.F. Goncharov, S.N. Tkachev, P. Dera, V.B. Prakapenka, Vibrational, elastic, and structural properties of cubic silicon carbide under pressure up to 75 GPa: Implication for a primary pressure scale, J. Appl. Phys. 113 (2013) 113503.
[52] R.A. Forman, G.J. Piermarini, J.D. Barnett, S. Block, Pressure measurement made by the utilization of ruby sharp-line luminescence, Science 176 (1972) 284.
[53] I.V. Aleksandrov, A.F. Goncharov, A.N. Zisman, S.M. Stishov, Diamond at high pressures: Raman scattering, equation of state, and high pressure scale, Sov. Phys. JETP 66 (1987) 384.
[54] W.B. Holzapfel, Refinement of the ruby luminescence pressure scale, J. Appl. Phys. 93 (2003) 1813.
[55] K. Kunc, I. Loa, K. Syassen, Diamond under pressure: *Ab-initio* calculations of the equation of state and optical phonon frequency revisited, High Press. Res. 24 (2004) 101.
[56] A. Dewaele, P. Loubeyre, M. Mezouar, Equations of state of six metals above 94 GPa, Phys. Rev. B 70 (2004) 094112.
[57] A. Dewaele, M. Torrent, P. Loubeyre, M. Mezouar, Compression curves of transition metals in the Mbar range: experiments and projector augmented-wave calculations, Phys. Rev. B 78 (2008) 104112.
[58] A.D. Chijioke, W.J. Nellis, I.F. Silvera, High-pressure equations of state of Al, Cu, Ta, and W, J. Appl. Phys. 98 (2005) 073526.
[59] L. Liu, Y. Bi, J. Xu, Ruby fluorescence pressure scale: revisited, Chin. Phys. B 22 (2013) 056201.
[60] S.D. Jacobsen, C.M. Holl, K.A. Adams, R.A. Fischer, E.S. Martin, et al., Compression of single-crystal magnesium oxide to 118 GPa and a ruby pressure gauge for helium pressure media, Am. Mineral. 93 (2008) 1823.
[61] Y. Bi, J. Xu, A Corrected Absolute MgO Pressure Scale up to 65 GPa and the Accuracy of Pressure Determination, unpublished, 2011.
[62] S. Sinogeikin, J. Bass, V. Prakapenka, D. Lakshtanov, G. Shen, et al., Brillouin spectrometer interfaced with synchrotron radiation for simultaneous X-ray density and acoustic velocity measurements, Rev. Sci. Instrum. 77 (2006) 103905.
[63] F. Datchi, A. Dewaele, P. Loubeyre, R. Letoullec, Y. LeGodec, et al., Optical pressure sensors for high-pressure-high-temperature studies in a diamond anvil cell, High Press. Res. 27 (2007) 447.
[64] C.S. Zha, W.A. Bassett, Internal resistive heating in diamond anvil cell for in situ X-ray diffraction and Raman scattering, Rev. Sci. Instrum. 74 (2003) 1255.
[65] J. Xu, H.K. Mao, P.M. Bell, Position-sensitive x-ray diffraction: hydrostatic compressibility of argon, tantalum, and copper 769 kbar, High Temperature-High Press. 16 (1984) 495.

[66] J. Xu, E. Huang, J. Lin, L. Xu, Raman study at high pressure and the thermodynamic properties of corundum: application of Kieffer's model, Am. Mineral. 80 (1995) 1157.
[67] L.S. Dubrovinsky, N.A. Dubrovinskaia, T. Le Bihan, Aggregate sound velocities and acoustic Grüneisen parameter of iron up to 300 GPa and 1200 K, PNAS 98 (2001) 9484.
[68] T. Kenichi, Evaluation of the hydrostaticity of a helium-pressure medium with powder X-ray diffraction techniques, J. Appl. Phys. 89 (2001) 662.
[69] R.J. Angel, M. Bujak, J. Zhao, G.D. Gatta, S.D. Jacobsen, Effective hydrostaticity limits pf pressure media for high-pressure crystallographic studies, J. Appl. Crystallogr. 40 (2007) 26.
[70] Q. Jing, Y. Bi, Q. Wu, F. Jing, Z. Wang, et al., Yield strength of molybdenum at high pressures, Rev. Sci. Instrum. 78 (2007) 073906.
[71] A.K. Singh, The lattice strains in specimen (cubic system) compressed nonhydrostatically in an opposed anvil device, J. Appl. Phys. 73 (1993) 4278.
[72] A.K. Singh, C. Balasigh, The lattice strains in a specimen (hexagonal system) compressed nonhydrostatically in an opposed anvil high pressure setup, J. Appl. Phys. 75 (1994) 4956.
[73] A.K. Singh, C. Balasigh, H.K. Mao, R.J. Hemley, J. Shu, Analysis of lattice strains measured under nonhydrostatic pressure, J. Appl. Phys. 83 (1998) 7567.
[74] A.K. Singh, T. Kenichi, Measurement and analysis of nonhydrostatic lattice strain component in niobium to 145 GPa under various fluid pressure-transmitting media, J. Appl. Phys. 90 (2001) 3269.
[75] T. Uchida, N. Funamori, T. Yagi, Lattice strains in crystals under uniaxial stress field, J. Appl. Phys. 80 (1996) 739.
[76] D. He, T.S. Duffy, X-ray diffraction study of the static strength of tungsten to 69 GPa, Phys. Rev. B 73 (2006) 134106.
[77] T.S. Duffy, G. Shen, J. Shu, H.K. Mao, R.J. Hemley, et al., Elasticity, shear strength, and equation of state of molybdenum and gold from x-ray diffraction under nonhydrostatic compression to 24 GPa, J. Appl. Phys. 86 (1999) 6729.
[78] R.J. Hemley, H.K. Mao, G. Shen, J. Badro, P. Gillet, et al., X-ray imaging of stress and strain of diamond, iron, and tungsten at megabar pressures, Science 276 (1997) 1242.
[79] A.K. Singh, H.K. Mao, J. Shu, R. Hemley, Estimation of single-crystal elastic moduli from polycrystalline X-ray diffraction at high pressure: application to FeO and iron, Phys. Rev. Lett. 80 (1998) 2157.
[80] H.K. Mao, J. Shu, G. Shen, R.J. Hemley, B. Li, et al., Elasticity and rheology of iron above 220 GPa and the nature of the Earth's inner core, Nature 396 (1998) 741.
[81] A.K. Singh, Analysis of nonhydrostatic high-pressure diffraction data (cubic system): assessment of various assumptions in the theory, J. Appl. Phys. 106 (2009) 043514.
[82] S. Karato, Theory of lattice strain in a material undergoing plastic deformation: Basic formulation and applications to a cubic crystal, Phys. Rev. B 79 (2009) 214106.
[83] P.A. Turner, C.N. Tome, A study of residual-stresses in zircaloy-2 with rod texture, Acta Metall. Mater. 42 (1994) 4143.
[84] B. Clausen, T. Lorentzen, T. Leffers, Self-consistent modeling of the plastic-deformation of fcc polycrystals and its implications for diffraction measurements of internal-stresses, Acta Mater. 46 (1998) 3087.
[85] D.J. Weidner, L. Li, M. Davis, J.H. Chen, Effect of plasticity on elastic-modulus measurements, Geophys. Res. Lett. 31 (2004) 6621.
[86] L. Li, D.J. Weidner, J.H. Chen, M.T. Vaughan, M. Davis, et al., X-ray strain analysis at high pressure: effect of plastic deformation in MgO, J. Appl. Phys. 95 (2004) 8357.
[87] S. Merkel, C. Tome, H.R. Wenk, Modeling analysis of the influence of plasticity on high pressure deformation of hcp. Co, Phys. Rev. B 79 (2009) 064110.
[88] H.K. Mao, J. Badro, J. Shu, R.J. Hemley, A.K. Singh, Strength, anisotropy, and preferred orientation of solid argon at high pressures, J. Phys. Condens. Matter 18 (2006) S963.
[89] E. Menendez-Proupin, A.K. Singh, *Ab initio* calculations of elastic properties of compressed Pt, Phys. Rev. B 76 (2007) 054117.
[90] K.W. Katahara, M.H. Manghnani, E.S. Fisher, Pressure derivatives of the elastic moduli of bcc titanium-vanadium-chromium, niobium-molybdenum and tantalum-tungsten alloys, J. Phys. F 9 (1979) 773.
[91] L. Liu, H.X. Song, H.Y. Geng, Y. Bi, J. Xu, Compressive behaviors of bcc bismuth up to 55 GPa, Phys. Status Solidi B 250 (2013) 1398.
[92] L. Liu, H.X. Song, Z.G. Wang, H.Y. Geng, Q. Jing, et al., Strength and equation of state of fluorite phase CeO_2 under high pressures, J. Appl. Phys. 112 (2012) 013532.
[93] J.I. Langford, X-ray powder diffraction studies of vitromet samples, J. Appl. Crystallogr. 4 (1971) 159.
[94] A.K. Singh, H.P. Liermann, Y. Akahama, H. Kawamura, Aluminum as a pressure-transmitting medium cum pressure standard for X-ray diffraction experiments to 200 GPa with diamond anvil cell, J. Appl. Phys. 101 (2007) 123526.
[95] A.K. Singh, H.P. Liermann, S.K. Saxena, Strength of magnesium oxide under high pressure: evidence for the grain-size dependence, Solid State Commun. 132 (2004) 795.
[96] A.K. Singh, H.P. Liermann, S.K. Saxena, H.K. Mao, U. Devi, Nonhydrostatic compression of gold powder to 60 GPa in a diamond anvil cell: estimation of compressive strength from X-ray diffraction data, J. Phys. Condens. Matter 18 (2006) S969.
[97] A.K. Singh, X-ray diffraction from solids under nonhydrostatic compression-some recent studies, J. Phys. Chem. Solids 65 (2004) 1589.
[98] Z. Wang, S.K. Saxena, V. Pischedda, H.P. Liermann, C.S. Zha, In situ X-ray diffraction study of the pressure-induced phase transformation in nanocrystalline CeO_2, Phys. Rev. B 64 (2001) 012102.
[99] L. Gerward, J.S. Olsen, L. Petit, G. Valitheeswaran, V. Kanchana, et al., Bulk modulus of CeO_2 and PrO_2-an experimental and theoretical study, J. Alloys Compd. 400 (2005) 56.
[100] M.I. Eremets, High Pressure Experimental Methods, Oxford University Press, Oxford, 1996, p. 761.
[101] B. Chen, A.E. Gleason, J.Y. Yan, K.J. Koski, S. Clark, et al., Elasticity, strength, and refractive index of argon at high pressure, Phys. Rev. B 81 (2010) 144110.
[102] H. Marquardt, S. Speziale, A. Gleason, S. Sinogeikin, I. Kantor, et al., Brillouin scattering and X-ray diffraction of solid argon to 65 GPa and 700 K: Shear strength of argon at HP/HT, J. Appl. Phys. 114 (2013) 093517.